




Hierarchically porous carbon with pentagon defects as highly efficient catalyst for oxygen reduction and oxygen evolution reactions

Zhaowei Zeng¹, Lei Yi¹, Jianwei He¹, Qian Hu¹, Yucong Liao¹, Yadong Wang^{1,*} , Wenbin Luo^{2,*}, and Mu Pan¹

¹ State Key Laboratory of Advanced Technology for Materials Synthesis and Processing, Wuhan University of Technology, 430070 Wuhan, China

² College of Materials Science and Engineering, Changsha University of Science and Technology, 410114 Changsha, China

Received: 22 November 2019

Accepted: 21 December 2019

Published online:

3 January 2020

© Springer Science+Business Media, LLC, part of Springer Nature 2020

ABSTRACT

Highly dispersed electrocatalysts and single-atom catalysts receive extensive attention in the field of multiple reactions involving water splitting, oxygen reduction, and CO₂ reduction. Herein, we develop a Fe/N co-doped hierarchically structured porous carbon (Fe/N/C-DT) by the dual-templating approach, involving the incorporation of ferrocenecarboxaldehyde (Fc-CHO) into the polyimide, followed by carbonization at 900 °C and etching. A steric hindrance offered by the ferrocene and the porosity of the obtained nanostructure prevent the aggregation of Fe atoms, resulting in the maximization of catalytic efficiency of iron-based sites. FeCl₂/N/C-DT and FeSO₄/N/C-DT using FeCl₂ and FeSO₄ as iron sources, respectively, are prepared for comparison, to further confirm the potential positive effect of Fc-CHO and explore the synergistic effect of the pentagon defects and Fe-N₄ on the catalytic performance in oxygen reduction reaction (ORR). The prepared Fe/N/C-DT exhibits outstanding electrochemical activity toward ORR ($E_{1/2} = 0.902$ V vs RHE) and impressive OER activity ($E_{j=10} = 1.66$ V) in alkaline conditions. The rechargeable Zn-air battery using Fe/N/C-DT as a cathode catalyst shows a peak power density of 220 mW cm⁻² and a high open-circuit voltage of 1.451 V in the all-solid-state Zn-air battery.

Introduction

The development of next-generation energy conversion and storage devices is the key for the sustainable development of human society due to the rapid

consumption of fossil fuels and the concomitant environmental contamination [1]. The oxygen reduction reaction (ORR) is a fundamental reaction in electrochemical devices, such as fuel cells and other renewable energy devices, e.g., metal-air batteries [2, 3]. Although Pt and a series of Pt-based alloys

Address correspondence to E-mail: ywang@whut.edu.cn; wenbin.luo@hotmail.com

have been well developed and proven to be the most efficient catalysts, the excessive price, scarcity, and the low durability limit their large-scale applications [4]. Therefore, inexpensive and efficient electrocatalysts are urgently needed to enter into widespread commercialization in energy sectors, such as energy-based transportation.

Iron-based carbon materials, as non-precious metal-based catalysts (NMPCs), exhibit high electrocatalytic activity in ORR and high chemical stability in both alkaline and acidic conditions [5]. Nevertheless, most of the highly efficient Fe-based catalysts often contain various Fe species (e.g., Fe-N_x, Fe/Fe₃C, Fe₃O₄@C) [6, 7]. In particular, the active sites, such as FeN₄, which are embedded in the sp² carbon lattice or located at the edges bridging the two graphene planes, have shown great potential, based on both theory and experimental data from X-ray absorption, X-ray photoelectron, and Mössbauer spectroscopy [8, 9]. Rational design and preparation of Fe-based electrocatalysts with homogeneous dispersion of the active sites are highly encouraged aiming to understand the active sites and thus to maximize the catalytic efficiency of the iron atom [10–12].

Increasing the number of available active sites and the intrinsic activity of the active site are the two main strategies promoting the increase in catalyst activity [13]. Hierarchically porous carbon (HPC) is widely used in the fields of gas adsorption, gas storage, heterogeneous catalysis, supercapacitors, and batteries [14–16]. The HPC, exhibiting a good electrical conductivity, acts as a suitable coordination environment for the iron atoms in which the distribution of Fe sites can be highly homogeneous, even at atomic scale [10, 17]. More active sites are exposed by optimizing HPC structure. The transport of electrons between metal atoms/nanoparticles and a suitable supports results in the charge redistribution, promoting the adsorption of oxygen molecules and reaction intermediates, and thus achieving a highly efficient oxygen reduction reaction [18]. Over the past decade, great efforts have been made to develop HPC supports of various morphologies [19–23]. Abundant studies have revealed that heteroatom doping (e.g., N, B, S, P) can change the electronic structure of the doped carbon material, making the oxygen reduction reaction easier [24–26]. Heteroatom doping can also change the electronic structure of Fe/N/C and has a positive effect on ORR performance [27]. Recently, Mu's group verified the influence of intrinsic

pentagon defects in the basal plane on the local electronic redistribution and the contraction of bandgap by theoretical calculations and experiments, which has an impact on the binding affinity of carbon matrix and electrochemical performance [28]. The pentagon defects may have a certain influence on the electronic distribution of Fe-N₄; therefore, it is meaningful to explore the effect of the pentagon carbon on the Fe-N₄ active center.

Herein, we report a facile dual-templating approach to synthesize a hierarchically structured porous carbon (Fe/N/C-DT) with Fe-N₄ active sites by incorporating ferrocenecarboxaldehyde (Fc-CHO) into the polyimide molecular chain directly. Ten nm of silicon dioxide and zinc acetate are used as dual templates. When the temperature was raised to be about 180 °C, Zn(CH₃COO)₂ was decomposed to be zinc oxide, and then was reduced to be Zn through further annealing at 900 °C. The formed reduced zinc will be evaporated at this high temperature (Eq. S1) [19]. The following HF etching will easily remove SiO₂ template. The prepared Fe/N/C-DT exhibits HPC with carbon nanotube structure, which will provide a larger surface area and more active sites. The iron precursor is a stable ferrocene derivative that can maintain an iron center that has the saturated electronic structure of krypton up to 400 °C [29], which may offer a steric hindrance for iron atoms distribution. In Fe/N/C-DT, some inevitable iron nanoparticles induced SiO₂ to grow CNTs during pyrolysis, which provides a high mesoporosity and higher conductivity, which enhanced the catalytic activity. The ferrocene with two cyclopentadienyl ligands preferably forms a pentagon carbon around Fe-N₄ after calcination. And by comparing with FeCl₂/N/C-DT and FeSO₄/N/C-DT, the advantage of Fc-CHO as an iron source is highlighted. This is the first report on the incorporation of ferrocene derivatives into the PI polymer aiming to synthesize highly dispersed Fe-N_x/C NMPCs catalysts, and through the calculation and experiments, the synergistic effects of pentagon carbon and Fe-N₄ on the catalytic performance were explored.

Experimental

Chemicals

NMP (1-methyl-2-pyrrolidinone), HF (hydrofluoric acid), FeCl₂·4H₂O, and MA (melamine) were

purchased from Sinopharm Chemical Reagent Co., Ltd., and used without any further purification. Fc-CHO (ferrocenecarboxaldehyde), PMDA (pyromellitic dianhydride), zinc acetate, $\text{FeSO}_4 \cdot 7\text{H}_2\text{O}$, and silicon dioxide were purchased from Shanghai Aladdin Biochemical Technology Co., Ltd.

Electrocatalyst preparation

Preparation of Fe/N/C-DT PMDA (3.9658 g, 18 mmol), MA (1.5861 g, 12.45 mmol), Fc-CHO (0.2948 g, 1.35 mmol), and [zinc acetate (0.7 g), 10 nm silicon dioxide (0.45 g)] were added to a 100-mL two-neck round-bottom flask equipped with a reflux condenser. After the addition of 30 mL NMP, the system was degassed by bubbling with nitrogen for 30 min. The homogeneous mixture was refluxed under inert atmosphere at 180 °C for 4 h. The reaction was initially accompanied by a white smoke, and the end product was a black gel. The system was cooled at room temperature under inert atmosphere. The black gel was dried under vacuum at 140 °C for 10 h to obtain a black solid. The black product was simply ground to form a powder, which was poured into a porcelain crucible and placed in a tube furnace. After that, the material was heated at 240 °C with a rate of 5 °C min^{-1} in N_2 for 2 h to achieve the complete imidization between melamine and PMDA. The intermediate product was subjected to a second pyrolysis treatment at 900 °C (rate of 5 °C min^{-1}) in N_2 for 2 h. After the tube furnace was cooled at room temperature, the obtained carbon material was taken out to the centrifuge tube. Then, the silica template was removed by soaking in hydrofluoric acid (30 mL) overnight at room temperature. The solid was washed ten times with deionized water to remove the residual impurities. The final product was dried in vacuum oven at 80 °C for 10 h to obtain a dark powder (1.5206 g, yield of 26%). The catalyst was denoted as Fe/N/C-DT. CHNSO element analysis and ICP analysis: Fe 0.565%, N 2.82%, C 85.77%, H 1.254%, Zn 0.093%.

Preparation of Fe/N/C and N/C-DT For the synthesis of Fe/N/C, the protocol was similar to that for Fe/C/N-DT except the use of the dual template. For the synthesis of the sample without iron (Fc-CHO), other steps were unchanged, but the second pyrolysis step was performed at 900 °C for 2 h. The sample was labeled as N/C-DT.

Preparation of $\text{FeSO}_4/\text{N/C-DT}$ and $\text{FeCl}_2/\text{N/C-DT}$ In the synthesis of these two samples, Fc-CHO is replaced by $\text{FeSO}_4 \cdot 7\text{H}_2\text{O}$ and $\text{FeCl}_2 \cdot 4\text{H}_2\text{O}$ on an equimolar basis, without changing the protocol used for Fe/N/C-DT. The samples were labeled as $\text{FeSO}_4/\text{N/C-DT}$ and $\text{FeCl}_2/\text{N/C-DT}$, respectively.

Materials characterization

Scanning electron microscopy (SEM) images were recorded on a JEM-7500F. Transmission electron microscopy (TEM) was performed on a JEM-1400Plus at 120 kV. High-resolution transmission electron microscopy (HRTEM) images and elemental mapping were performed on a Talos F200S. Fourier transform infrared spectroscopy (FTIR) was performed on a Nicolet 6700 FTIR spectrometer. Thermogravimetric analysis was performed on a STA449C analyzer in the temperature range from 20 to 1000 °C. The inductively coupled plasma optical emission spectrometry (ICP-OES) measurement was conducted on Prodigy 7 elemental analyzer. Elemental analysis (CHNSO) was performed on a Vario EL cube. Powder X-ray diffraction (PXRD) patterns were recorded on a RU-200B/D/MAX-RB diffractometer from 10° to 80°. Raman spectra were recorded on an inVia Renishaw Raman microscope. X-ray photoelectron spectroscopy experiments (XPS) were conducted on a Thermo ESCALAB 250XI. N_2 adsorption/desorption measurements were measured on ASAP 2020 M fully automatic surface area and porosity analyzer.

Electrocatalytic testing

Electrochemical performance measurements of all catalysts were performed on a CHI660E electrochemical workstation. Reversible hydrogen electrode (RHE) was used as the reference electrode, carbon electrode was used as the counter electrode, and the glassy carbon electrode (5.0 mm diameter) coated with the catalyst was used as the working electrode. The working electrode was polished with alumina powder of different particle sizes, then washed with deionized water, and dried at room temperature. The test temperature was controlled at 25 °C. For the electrochemical measurement in alkaline electrolytes, N_2/O_2 -saturated 0.1 M KOH solution was used. The catalyst ink was prepared by dispersing 6 mg catalysts into a mixed solution of 1 mL of water/ethanol

($V_{\text{water}}/V_{\text{ethanol}} = 9:1$) and 20 μL of Nafion (5 wt%) in an ultrasonic ice bath. Then, 22 μL of as-prepared slurry was dropped onto the surface of the polished glassy carbon electrode, and let it dry for 30 min at room temperature. As for the commercial Pt/C ink, 3 mg Pt/C dispersed in the same solution and 10 mL ink were coated on the surface of RDE.

Zn–air battery tests

The liquid Zn–air battery was constructed of carbon paper (as the air cathode), Zn foil (as the anode), and electrolyte (a mixed aqueous solution of 6 M KOH and 0.2 M Zn^{2+}). The Zn foil (10 \times 20 mm) was washed with ethanol. The carbon paper (10 \times 20 mm) was coated with about 1 mg cm^{-2} catalyst on an area of 10 \times 10 mm. A home-made all-solid-state Zn–air battery with three components was fabricated (Fig. 5d). The PVA membrane was prepared as follows: 4.5 g PVA powder was added to 45 mL deionized water and stirred at 95 $^{\circ}\text{C}$ for at least 40 min. After the mixture was cooled at room temperature, it turned into a transparent gel. Then, 4 mL of 18 M KOH solution and 0.2 M zinc acetate solution were added. After stirring for 30 min, the transparent gel was poured onto a suitable glass dish and freeze-dried in a refrigerator overnight. After heating at 60 $^{\circ}\text{C}$, a PVA membrane of a 1 mm thick and dimension of 25 \times 25 mm was cut. The catalyst (2 mg cm^{-2}) was added dropwise into a 20 \times 20 mm central region of the membrane.

Results and discussion

Morphology and structural characterization

A typical route of the synthetic process of Fe/N/C-DT is shown in Fig. 1a. PMDA (pyromellitic dianhydride) reacts with $-\text{NH}_2$ in MA (melamine) to form PI (polyimide) [30]. Fc-CHO is then incorporated into the network of the resulted PI in a catalyst free manner and based on the Schiff base chemistry [31]. Fourier transform infrared spectrometry was used to analyze the ferrocene-based polymer structure. In the FTIR spectrum of Fc-MA-PMDA (denoting the synthesized Fe/N/C-DT without pyrolysis and dual-template) (Fig. S1), the characteristic bands at 3469 and 3419 cm^{-1} of the free amine group in MA and the stretching band of aldehyde groups in Fc-CHO at

1679 cm^{-1} are invisible. The two bands at 1770 and 1859 cm^{-1} ascribed to the stretching vibrations of the carbonyl in phase and out of phase in PMDA are not visible, as well. Instead, Fc-MA-PMDA shows characteristic vibration bands of imine ring obtained by the reaction of $-\text{NH}_2$ in MA with the anhydride group in PMDA, which appeared at 1787, 1729, and 1360 cm^{-1} . These bands can be ascribed to the in-phase (or symmetric) stretching vibration of two carbonyl groups on the five-membered imine ring of polyimide, corresponding to the reversed (or asymmetric) carbonyl stretching vibration and strong stretching vibration of C–N–C, respectively. Because of the Schiff base chemistry reaction, new stretching vibration bands corresponding to the secondary amine (N–H) and methylimine group ($-\text{C}=\text{N}-$) were observed at 3430 and 1625 cm^{-1} , respectively, suggesting the successful condensation reaction of Fc-CHO with MA. In summary, the disappearance of the original functional groups ($-\text{NH}_2$, $-\text{CHO}$, carbonyl) and the formation of the new groups ($-\text{NH}-$, imine ring) indicate the successful synthesis of the target product.

Thermogravimetric analysis was performed in a N_2 atmosphere between 25 and 1000 $^{\circ}\text{C}$ with heating rate of 5 $^{\circ}\text{C min}^{-1}$. The recorded TG curve is displayed in Fig. S2 and demonstrates the evolution mechanism of Fc-MA-PMDA-DT (denoting the synthesized Fe/N/C-DT without pyrolysis). TG curve can be divided into several ranges of mass loss. The weight loss of 18% in the temperature range of 100–200 $^{\circ}\text{C}$ is due to the evaporation of the residual solvent NMP (1-Methyl-2-pyrrolidinone) adsorbed in the porous structure and decomposition of zinc acetate. Due to the imidization process and further crosslinking of the polymer, an obviously weight loss of 9% appeared in the range from 200 to 300 $^{\circ}\text{C}$. A sharp weight loss of 47% occurred in the temperature range from 300–620 $^{\circ}\text{C}$ attributed to the decomposition and carbonization of polymer. Further graphitization leads to a weight loss at the temperature from 620–900 $^{\circ}\text{C}$. A small weight loss was also observed above 900 $^{\circ}\text{C}$ due to the volatilization of zinc template.

The as-prepared Fe/N/C-DT showed obvious graphite-like structure with a hierarchically porous structure, as demonstrated by the scanning electron microscopy (SEM) images (Fig. 1b and Fig. S3 a, b). The formation of a hierarchically porous structure in Fe/N/C-DT was also confirmed by the

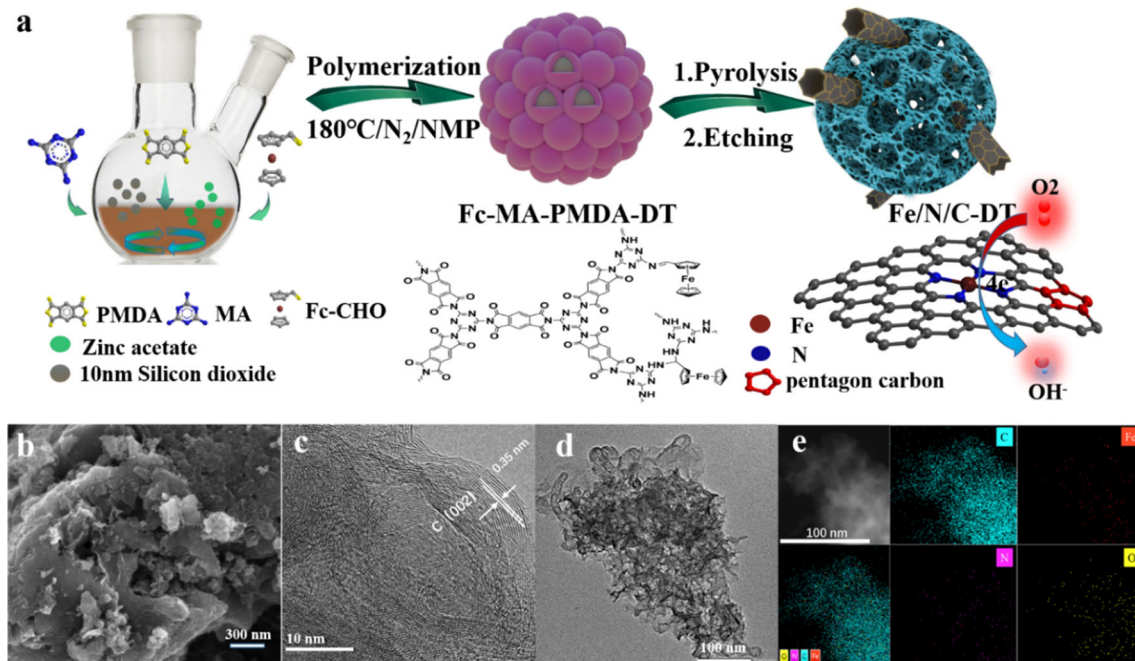


Figure 1 a Schematic illustration of the synthesis of Fe/N/C-DT; b SEM image, c high-resolution TEM (HRTEM) image, d TEM images of Fe/N/C-DT with e HAADF-STEM and EDS mapping images.

corresponding images of transmission electron microscopy (TEM) images (Fig. 1d and Fig. S3 c, d) and high-resolution TEM images (Fig. S4a). In TEM images, Fe/N/C-DT showed the hierarchically porous structure consisting of uniform mesopores with a diameter of ~ 10 nm and carbon nanotubes with a diameter of 12.2 nm crossing the nanostructure (Fig. S4b). Fe/N/C (denoting Fe/N/C synthesized through similar processes but without a dual template) exhibited a porous structure with fish scale-like mesoporous structure, but significant Fe aggregation appeared and no carbon nanotubes were found (Fig. S5a, b). HAADF-STEM and EDS mappings (Fig. 1e) Fe/N/C-DT showed that C, N, Fe, O are uniformly distributed throughout the nanostructure without traces of aggregation of iron nanoparticles.

To gain further insight into the structure of the pyrolysis products, powder X-ray diffraction (XRD) (Fig. S6a) was used. The diffractogram of N/C-DT (denoting N/C-DT synthesized by a similar processes as for Fe/N/C-DT but without Fc-CHO) displays a peak at 26° , which is assigned to the (002) reflection of graphitic carbon, consistent with the corresponding TEM (Fig. S7b). The X-ray patterns of Fe/N/C and Fe/N/C-DT display a sharper and stronger diffraction peak at 26° and a weak peak at 44° , corresponding to the graphite (100)/(101)

reflections of graphitic carbon. These changes in the diffractogram suggest a crystallization process induced by evenly dispersed iron incorporation resulting in a higher graphitic degree since iron atoms is an efficient catalyst for the production of graphene. The high-resolution TEM (HRTEM) image (Fig. 1c) further reveals that Fe/N/C-DT has a high graphitization degree with a lattice spacing of 0.35 nm. This improved graphitization degree will greatly accelerate the electron transfer, and thus the ORR performance will be enhanced [32]. Interestingly, no obvious diffraction peaks assigned to crystalline Fe_3C and metallic Fe are observed, indicating a high dispersion of Fe species confined in Fe/N/C-DT. By contrary, the diffractogram of Fe/N/C sample with similar low content of iron displayed the peaks at 42.886° , 43.751° and 44.989° , characteristic to iron carbide phase (JCPDS card: No. 85-1317). As shown in Fig. S6b, displaying the Raman spectra of Fe/N/C-DT and Fe/N/C, D and G bands at 1330 and 1580 cm^{-1} , respectively, the intensity ratio of D band and G band (I_D/I_G) was used to estimate the defects in graphitic carbon [33]. The I_D/I_G ratio for Fe/N/C-DT is 1.15, but it decreases to 1.12 in Fe/N/C due to the higher graphitization induced by Fe aggregates during the high-temperature pyrolysis, indicating a larger number of defects in Fe/N/C-DT.

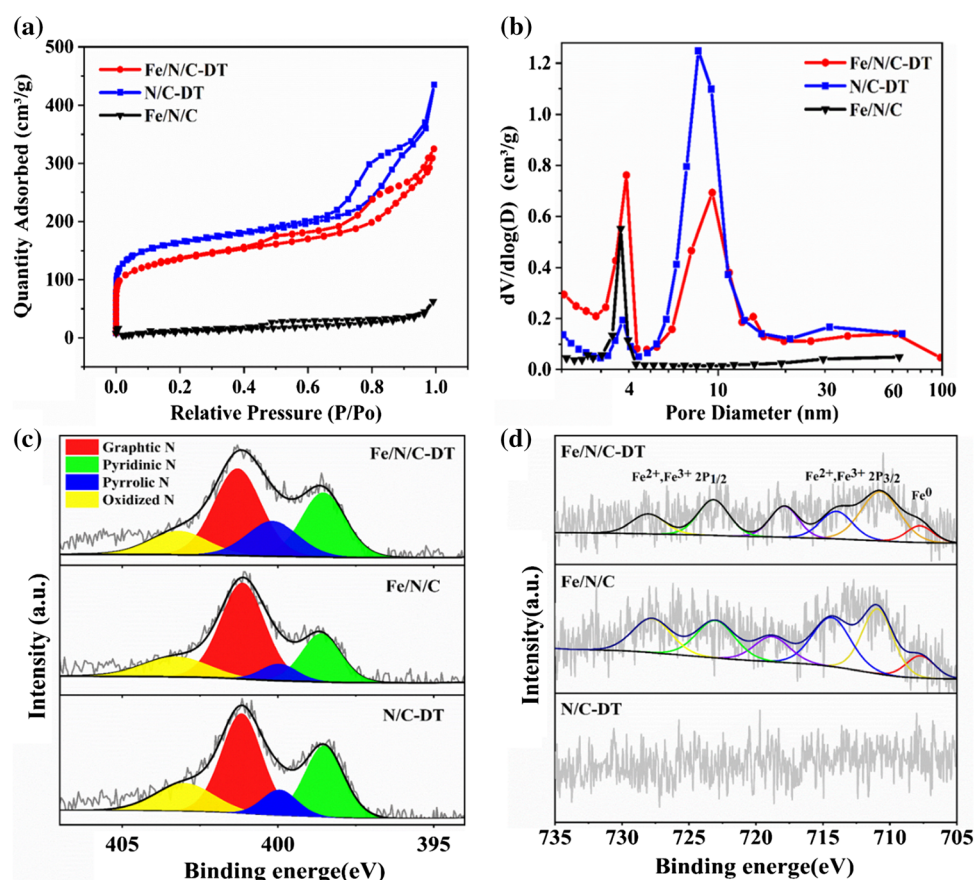
A broad 2D peak at 2642 cm^{-1} and D + G peak at 2900 cm^{-1} were observed in the spectra of Fe/N/C and Fe/N/C-DT samples, which indicate the simultaneous presence of some layered graphene-like architectures and D band.

The specific surface area and pore-size distribution of the pyrolysis products were investigated by N_2 adsorption/desorption measurement (Fig. 2a, b). The N_2 isotherms of Fe/N/C-DT and N/C-DT are a combination of type I and IV isotherms, revealing the existence of micropores and mesopores [34]. The BET surface areas of Fe/N/C-DT, N/C-DT, and Fe/N/C are 484, 586, and $35\text{ m}^2\text{ g}^{-1}$, respectively. The total pore volume of pores Fe/N/C-DT, N/C-DT, and Fe/N/C are 0.503, 0.673, and $0.097\text{ cm}^3\text{ g}^{-1}$, respectively. Pore-size distribution curves show that Fe/N/C-DT and Fe/N/C possess more mesopores about 3 nm than N/C-DT, indicating that the reaction between Fe-CHO and MA introduced a large number of mesopores about 3 nm. Due to the addition of 10 nm SiO_2 , many mesopores of 10 nm are present in Fe/N/C-DT and N/C-DT, in line with the TEM results (Fig. 1d and Fig. S7a). This hierarchically porous

structure will benefit the enhancement of the electrocatalytic activity to ORR and OER. The rich microporosity of the as-synthesized catalyst will expose a large number of accessible active sites for electrocatalytic reaction; while the high mesoporosity is essential for the efficient mass transport in the catalyst layer [20]. Compared with Fe/N/C, Fe/N/C-DT with more active sites and a higher efficient mass transport efficiency will surely realize much improved electrochemical performance.

X-ray photoelectron spectroscopic (XPS) measurements were further carried out to explore the elemental composition and chemical state at the sample surface. XPS survey spectrum of Fe/N/C-DT, Fe/N/C, N/C-DT (Fig. S8a) confirms the coexistence of carbon, oxygen, and nitrogen elements on the surface. On the other hand, ICP and EDS analyses showed a very low content of Fe in Fe/N/C-DT (0.565%) and Fe/N/C (0.65%) (Table S1 and Fig. S9), which explain the very small Fe2p peaks observed in survey spectra of all catalysts. The high-resolution N1s spectra of the three sample (Fig. 2c) were deconvoluted and fitted with four components (i.e.,

Figure 2 **a** N_2 adsorption–desorption isotherms and **b** pore-size distribution of Fe/N/C-DT, Fe/N/C, and N/C-DT; **c** N1s XPS spectra and **d** Fe2p XPS spectra of Fe/N/C-DT, Fe/N/C, and N/C-DT.



398.5, 400.1, 401.2, and 403.2 eV) assigned to pyridinic N, pyrrolic N, graphitic N, and oxidized N, respectively. Interestingly, the total content of pyridinic N and pyrrolic N species in Fe/N/C-DT dramatically increased in comparison with Fe/N/C and N/C-DT samples (Fig. S8b), which may improve ORR performance [35]. The high-resolution Fe2p spectra of Fe/N/C-DT and Fe/N/C were deconvoluted and fitted with six peaks (Fig. 2d), which correspond to Fe⁰ (707.8 eV), Fe2p_{3/2} (Fe²⁺, Fe³⁺ 710.7–714 eV), satellite peak (717.8 eV), and Fe2p_{1/2} (Fe²⁺, Fe³⁺ 728–723.2 eV), demonstrating the coexistence of Fe⁰, Fe²⁺, and Fe³⁺.

Electrochemical performance

The electrocatalytic performances of the as-prepared catalysts were first examined in O₂/N₂-saturated 0.1 M KOH solution on the rotating disk electrode (RDE) in a typical three-electrode system. As can be seen in Fig. 3a and Fig. S10a, Fe/N/C-DT displays an obvious strong oxygen reduction peak at 0.88 V. The two reduction peaks' current density at 0.74 and 0.76 V for Fe/N/C and N/C-DT is much lower. Linear sweep voltammetry (LSV) curves illustrated in Fig. 3b show that the half-wave potential of N/C-DT shifts from 0.78 to 0.902 V after the incorporation of Fe species, and the onset potential of Fe/N/C-DT (1.043 V) is 143 mV higher than that of N/C-DT (0.9 V). The Fe/N/C shows an inferior onset potential (E_{onset}) of 0.9 V and the half-wave potential of 0.731 V (Fig. 3b). Moreover, Fe/N/C-DT exhibits a higher diffusion-limited current density (5.93 mA cm⁻² at 0.4 V) than that of Pt/C (5.81 mA cm⁻² at 0.4 V). Koutecky–Levich (K–L) plots obtained from the LSV polarization curves at different rotation speeds are shown in Fig. 3c. The electron transfer number was calculated based on the Koutecky–Levich (K–L) equation. The average electron transfer number of Fe/N/C-DT is ~ 4.5, indicating a quasi-four-electron pathway for ORR. Furthermore, a low Tafel slope of 63 mV dec⁻¹ for Fe/N/C-DT (Fig. 3d), compared with that of Fe/N/C (114 mV dec⁻¹), N/C-DT (140 mV dec⁻¹), and 20% Pt/C (66 mV dec⁻¹), indicating that Fe/N/C-DT will show a smaller overpotential at the same current density, further proved that Fe/N/C-DT exhibits superior activity in ORR. Methanol-resistant activity of Fe/N/C-DT was also examined. There is no obvious change in the normalized current on Fe/N/

C-DT working electrode after an injection with 9 mL of methanol while Pt/C dropped immediately under the same conditions (Fig. 3e). Amperometric *i*-*t* tests were carried out to evaluate the electrochemical stability of the catalysts. Fe/N/C-DT exhibited significantly better stability (retention rate of 90%) than the benchmark Pt/C catalyst (retention rate of 73.6%) after 40000 s (Fig. 3f). We attributed the better performance of Fe/N/C-DT to the porosity of the obtained nanostructure and more active Fe sites.

As shown in Fig. S10b, the OER (oxygen evolution reaction) performances of Fe/N/C-DT in 1 M KOH solution were also tested using IrO₂ as a comparison. The operating potential delivering a current density of 10 mA cm⁻² ($E_{j=10}$) has usually been described as the OER activity benchmark [36]. The potential of Fe/N/C-DT (1.66 V) at 10 mA cm⁻² is just 77 mV higher than that of the commercial IrO₂ catalyst (1.58 V). The Tafel slope of Fe/N/C-DT is 170 mV dec⁻¹, which is higher than that of IrO₂ (56 mV dec⁻¹) (Fig. S10c). Nevertheless, the OER performance of Fe/N/C-DT is better than most of the previously reported NMPCs electrocatalysts (Table S2).

To further confirm the positive effect of Fc-CHO as an iron source for electrocatalysis, FeCl₂/N/C-DT and FeSO₄/N/C-DT using FeCl₂ and FeSO₄ as iron sources, respectively, were prepared for comparison. It was found that FeCl₂/N/C-DT, and FeSO₄/N/C-DT all exhibit almost the same hierarchically porous structure with the interpenetrated carbon nanotubes as Fe/N/C-DT. However, the carbon nanotube diameters are 12.2 nm for Fe/N/C-DT, 59 nm for FeCl₂/N/C-DT, and 151 nm for FeSO₄/N/C-DT (Fig. S4b, S11). It is well known that the diameter of CNTs is directly proportional to the size of the iron catalyst particle, which can indirectly confirm the positive effect of Fc-CHO on the uniform dispersion of iron atoms [37], and smaller carbon nanotubes diameters can carry more FeN_x active sites [38]. It is attributed to the steric hindrance effect of ferrocene in the polymer, which can largely alleviate the severe iron agglomeration. Since the structure and composition of the three samples are very similar, there are many similarities on XRD and XPS analysis (Fig. S12, S13, Fig. 4b). However, since the agglomeration of iron nanoparticles in FeCl₂/N/C-DT and FeSO₄/N/C-DT is more pronounced with respect to Fe/N/C-DT, the number of carbon nanotubes produced by iron-catalyzed silicon is higher and the diameter of the carbon nanotubes is larger, which indirectly leads

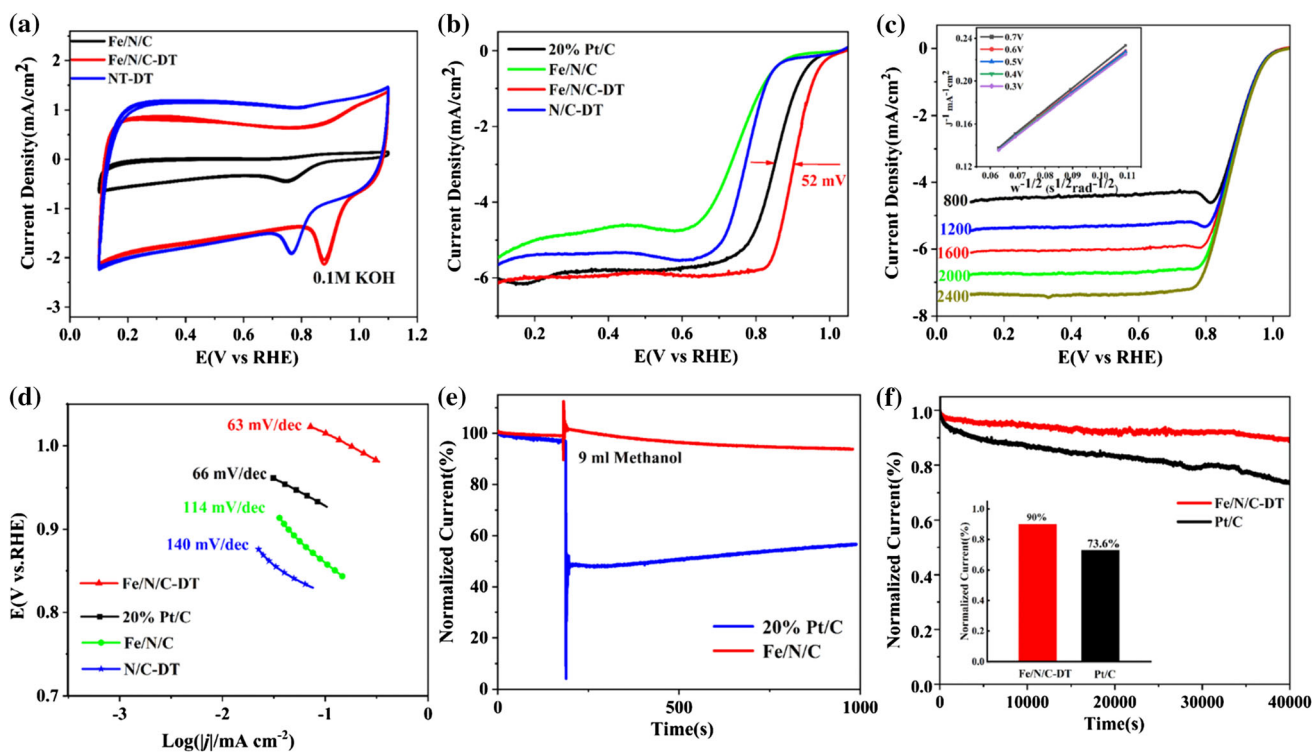


Figure 3 ORR performance of Fe/N/C-DT. **a** the cyclic voltammetry (CV) curves of Fe/N/C-DT, Fe/N/C, and N/C-DT in 0.1 M KOH saturated with O_2 at a sweep rate of 20 mV s^{-1} ; **b** ORR polarization curves of Fe/N/C-DT, Fe/N/C, N/C-DT, and 20% Pt/C at 1600 rpm and a sweep rate of 10 mV s^{-1} ; **c** polarization curves at different rotating rates (800–2400 rpm) at a sweep rate of 10 mV s^{-1} for Fe/N/C-DT (inset: corresponding

K–L plots (J^{-1} versus $W^{-1/2}$) at various potentials); **d** Tafel plots of Fe/N/C-DT, Fe/N/C, N/C-DT, and 20% Pt/C derived by the mass transport correction from the corresponding LSV data; **e** methanol-resistant test of Fe/N/C-DT and 20% Pt/C with 9 mL methanol injection; **f** The $i-t$ chronoamperometric responses of Fe/N/C-DT and 20% Pt/C at a constant voltage of 0.6 V (inset: retention rate after 40000 s).

to a decrease in the I_D/I_G . The I_D/I_G ratio decreased from 1.15 for Fe/N/C-DT to 1.05 and 1.02 for $FeCl_2/N/C$ -DT and $FeSO_4/N/C$ -DT, respectively, as shown in Fig. 4a. This indicates that Fe/N/C-DT exhibits higher defect density and more active sites than $FeCl_2/N/C$ -DT and $FeSO_4/N/C$ -DT.

Although the iron content is low and the noise of Fe2p XPS spectra is large, a series of smooth fitting curves of Fe/N/C-DT, $FeSO_4/N/C$ -DT, and Fe/N/C by the Savitzky–Golay smoothing method as shown in Fig. 4c. The signal at around 710 eV can be ascribed to Fe in Fe– N_x configuration [39]. For the $FeSO_4/N/C$ -DT and Fe/N/C samples, a significant positive shift of the signal of Fe– N_x was noticed. Higher binding energy means lower charge density on central Fe atoms, and large degree of interaction between Fe– N_x and Fe_3C leads to a decrease in the charge density of central Fe atom [6]. From this point of view, it can be proved that the degree of interaction between Fe– N_x and Fe_3C in Fe/N/C-DT is not as

prominent as in $FeSO_4/N/C$ -DT and Fe/N/C (perhaps because of the low content of Fe_3C , it is not easy to be detected in XRD), so the use of ferrocene and the dual-templating approach facilitates the formation of highly dispersed electrocatalysts, even at the atomic scale.

As can be seen from cyclic voltammetry (CV) curve (Fig. 4d), electrocatalysts with three different iron sources displayed a well-defined and similar ORR peak at potentials between 0.80 and 0.96 V in 0.1 M KOH. The linear sweep voltammetry (LSV) curves tested on RDE (Fig. 4e) show that the onset potentials of the three materials are nearly the same, but the half potential of Fe/N/C-DT is 26 mV higher than those of $FeCl_2/N/C$ -DT and $FeSO_4/N/C$ -DT. Fe/N/C-DT (63 mV dec^{-1}) also shows a significantly lower Tafel slope than those of other two reference catalysts (75 and 72 mV dec^{-1} , respectively) (Fig. 4f). Just as heteroatoms (N, B, O, P, S) doped with carbon, pentagon defects can also cause electron modulation to change

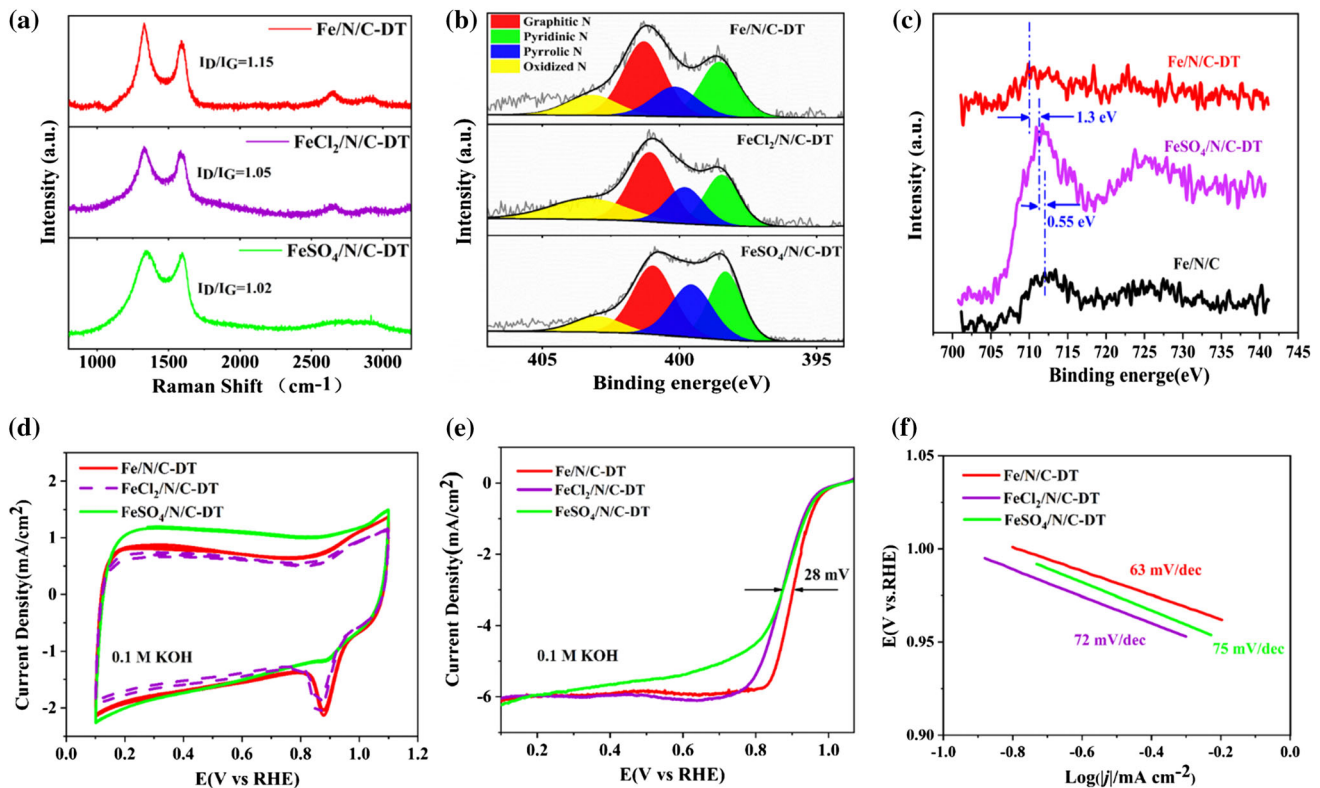


Figure 4 **a** Raman spectra, **b** N1s XPS spectra and **c** Fe2p XPS spectra of Fe/N/C-DT, FeCl₂/N/C-DT, and FeSO₄/N/C-DT. **d** The cyclic voltammetry (CV) curves, **e** LSV curves, and **f** the

corresponding Tafel plot of Fe/N/C-DT, FeSO₄/N/C-DT, and FeCl₂/N/C-DT in O₂/N₂-saturated 0.1 M KOH.

the charge distribution and electronic properties of carbon skeletons, which in turn affects their interaction with oxygen molecules and reaction intermediates for ORR [24–26]. Grafting the iron source to the polymer makes the active sites in the synthesized catalyst more uniformly dispersed. Under the same iron content, compared to FeCl₂/N/C-DT and FeSO₄/N/C-DT, Fe/N/C-DT has higher catalytic activity, undoubtedly.

DFT calculation and performance of Zn–air batteries

Calculations based on density functional theory (DFT) in Dmol3 code were performed on the four theoretical model structures (Fig. S14a, b, c, d), irregular graphene with all the common hexagon (C6), irregular graphene with a Fe–N₄ site, irregular graphene with a pentagon defect carbon on the edge, and irregular graphene with a Fe–N₄ site and a pentagon defect carbon (labeled as I-Gra, I-FeN₄, I-Pen, and I-FeN₄-Pen, respectively). The adsorption energies of oxygen, E_{ads} , of the four theoretical

models showed that I-FeN₄-Pen exhibits a higher oxygen adsorption energy (3.265 eV) than that of I-Gra (1.034 eV), I-FeN₄ (2.340 eV), and I-Pen (1.496 eV) (Fig. S14e, f, g, h, Fig. S15). The introduction of a pentagon defect-rich carbon can enhance the energy of O₂ adsorption, and the synergy between the pentagon carbon and Fe–N₄ strongly enhances the adsorption energy than Fe–N₄ active site alone. These results reveal that I-FeN₄-Pen accelerates the oxygen adsorption process and thus achieves an outstanding oxygen reduction performance [2, 40].

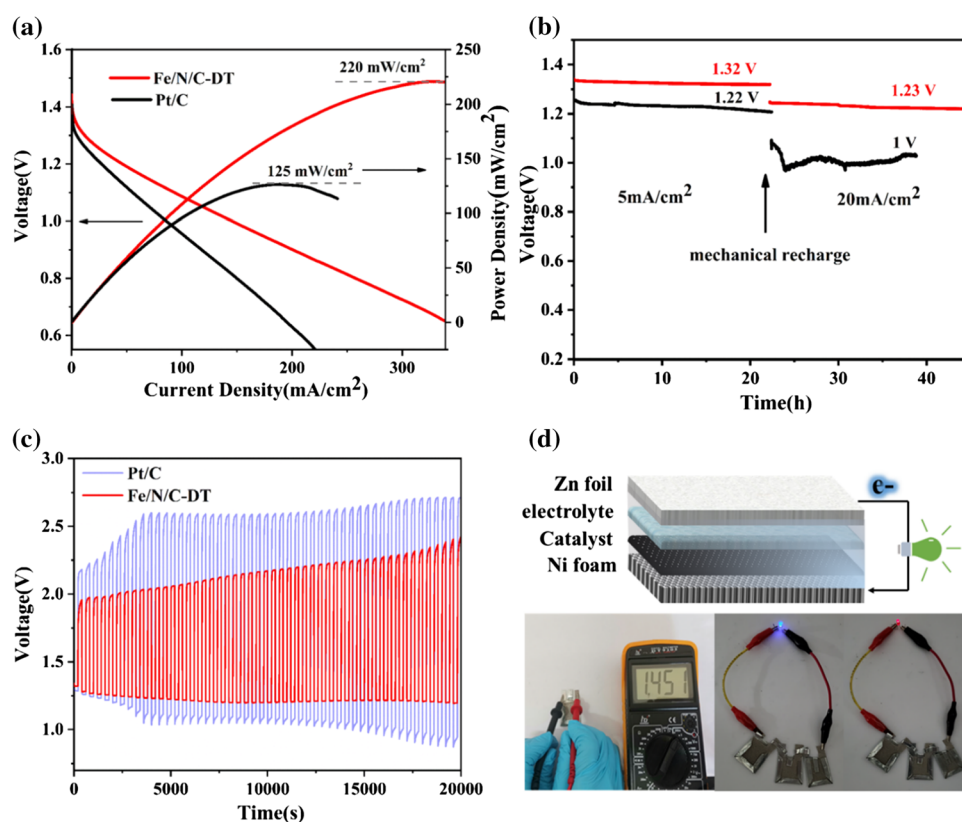
Knowing that Fe/N/C-DT presents an outstanding activity in ORR and considerable OER performance, and an O₂ electrode potential gap ΔE ($\Delta E = E_{j=10, OER} - E_{1/2, ORR}$) of 0.758 V, the possibility to use the oxygen electrodes for the reversible redox reaction is obvious [41]. Liquid Zn–air battery and all-solid-state Zn–air battery are assembled separately. In the liquid Zn–air battery, catalysts are loaded on the carbon paper acting as an air cathode, Fe/N/C-DT and the Pt/C catalysts were carried out under the same conditions. Fe/N/C-DT displays a higher open-circuit voltage (1.48 V) than that of Pt/C

(1.41 V) (Fig. S16). In discharge polarization curves and power density curves (Fig. 5a), Fe/N/C-DT displays a peak power density of 220 mW cm^{-2} , which far exceeds that of Pt/C (125 mW cm^{-2}). By replacing the zinc anode and electrolyte after a continuous discharge current density of 5 mA cm^{-2} for 20 h, the same electrode continues discharging at 20 mA cm^{-2} for 20 h. The output voltage of Fe/N/C-DT at a discharge current density of 5 and 20 mA cm^{-2} is more stable and higher than that of Pt/C (Fig. 5b). Due to the small potential gap, ΔE , a discharge–charge test at 5 mA cm^{-2} was conducted. A gradual increase in discharge–charge potential gap is observed for both Fe/N/C-DT air electrode and Pt/C air electrode (Fig. 5c). However, Fe/N/C-DT air electrode shows much better rechargeability. An all-solid-state Zn–air battery was constructed with Fe/N/C-DT catalyst coated nickel mesh as the air electrode (Fig. 5d). Remarkably, Fe/N/C-DT exhibits a high open-circuit voltage of 1.451 V. In addition, three such batteries in series can illuminate a 3-V light-emitting diode (LED) lamp.

Conclusions

In summary, we successfully developed a Fe/N/C-DT electrocatalyst via pyrolysis Fc–MA–PMDA polymer. The material was prepared by the dual-templating approach and incorporating the Fc–CHO to the PI polymer chain directly. The hierarchically porous carbon structure, resulted from the dual-templating approach, facilitated the uniform dispersion of the iron nanoparticles or even single Fe atom dispersion. The well-dispersed iron nanoparticles and the well-conducting carbon support promoted the electron exchange at the interface of metal atoms/nanoparticles and carbon supports, improving the adsorption energy of oxygen and the intermediate product, which further enhanced the electrocatalytic activity of the oxygen. DFT calculations showed that the synergistic effect of pentagon carbon and Fe–N₄ had a positive effect on catalyst performance in ORR. The prepared Fe/N/C-DT exhibited excellent ORR activity, superior stability, and impressive OER performance in alkaline media. Fe/N/C-DT driven by the liquid Zn–air battery possessed a higher peak power density, a higher open-circuit voltage, and a more stable discharge

Figure 5 Performance of “rechargeable” Zn–air batteries. **a** Discharge polarization and power density curves of Fe/N/C-DT and Pt/C; **b** The galvanostatic discharge curves of the liquid Zn–air batteries at 5 mA cm^{-2} , followed by discharge at 20 mA cm^{-2} . **c** Galvanostatic discharge–charge cycling curves at a current density of 5 mA cm^{-2} with 400 s cycle. **d** Schematic diagram of the all-solid-state zinc–air, a high open-circuit voltage of 1.451 V, three batteries in series illuminated a 3-V red and blue LED lamp.



than those of Pt/C. And all-solid-state Zn–air battery showed a high open-circuit voltage and feasible practical application. The novel design implying the incorporation of iron source with steric hindrance effect into the polymer could inspire the design of new electrocatalysts with the active sites dispersed at the atomic scale and boost the exploration of the impact of the pentagon defect-rich carbon on Fe–N₄.

Acknowledgements

The authors wish to acknowledge the National Natural Science Foundations of China (No. 21473128) for financial assistance.

Compliance with ethical standards

Conflict of interest The authors declare no conflict of interest.

Electronic supplementary material: The online version of this article (<https://doi.org/10.1007/s10853-019-04327-5>) contains supplementary material, which is available to authorized users.

References

- Seh ZW, Kibsgaard J, Dickens CF, Chorkendorff IB, Nørskov JK, Jaramillo TF (2017) Combining theory and experiment in electrocatalysis: insights into materials design. *Science* 355:eaad4998
- Nørskov JK, Rossmeisl J, Logadottir A, Lindqvist LR, Kitchin JR, Bligaard T, Jonsson H (2004) Origin of the overpotential for oxygen reduction at a fuel-cell cathode. *J Phys Chem B* 108:17886–17892
- Chen YN, Guo Y, Cui H, Xie Z, Zhang X, Wei J, Zhou Z (2018) Bifunctional electrocatalysts of MOF-derived Co–N/C on bamboo-like MnO nanowires for high-performance liquid-and solid-state Zn–air batteries. *J Mater Chem A* 6:9716–9722
- Zhang R, He S, Lu Y, Chen W (2015) Fe Co, N-functionalized carbon nanotubes in situ grown on 3D porous N-doped carbon foams as a noble metal-free catalyst for oxygen reduction. *J Mater Chem A* 3:3559–3567
- Yi JD, Xu R, Wu Q, Zhang T, Zang KT, Luo J, Liang YL, Huang YB, Cao R (2018) Atomically dispersed iron–nitrogen active sites within porphyrinic triazine-based frameworks for oxygen reduction reaction in both alkaline and acidic media. *ACS Energy Lett* 3:883–889
- Jiang WJ, Gu L, Li L, Zhang Y, Zhang X, Zhang LJ, Wang JQ, Hu JS, Wei Z, Wan LJ (2016) Understanding the high activity of Fe–N–C electrocatalysts in oxygen reduction: Fe/Fe₃C nanoparticles boost the activity of Fe–N_x. *J Am Chem Soc* 138(10):3570–3578
- Hadidi L, Davari E, Ivey DG, Veinot JG (2017) Microwave-assisted synthesis and prototype oxygen reduction electrocatalyst application of N-doped carbon-coated Fe₃O₄ nanorods. *Nanotechnology* 28:095707
- Zitolo A, Goellner V, Armel V, Sougrati MT, Mineva T, Stievano L, Fonda E, Jaouen F (2015) Identification of catalytic sites for oxygen reduction in iron-and nitrogen-doped graphene materials. *Nat Mater* 14:937
- Li J, Ghoshal S, Liang W, Sougrati MT, Jaouen F, Halevi B, McKinney S, McCool G, Ma C, Yuan X, Ma ZF (2016) Structural and mechanistic basis for the high activity of Fe–N–C catalysts toward oxygen reduction. *Energ Environ Sci* 9:2418–2432
- Su J, Ge R, Dong Y, Hao F, Chen L (2018) Recent progress in single-atom electrocatalysts: concept, synthesis, and applications in clean energy conversion. *J Mater Chem A* 6:14025–14042
- Mun Y, Kim MJ, Park SA, Lee E, Ye Y, Lee S, Kim YT, Kim S, Kim OH, Cho YH, Sung YE (2018) Soft-template synthesis of mesoporous non-precious metal catalyst with Fe–N_x/C active sites for oxygen reduction reaction in fuel cells. *Appl Catal B-Environ* 222:191–199
- Zhang Z, Sun J, Wang F, Dai L (2018) Efficient oxygen reduction reaction (ORR) catalysts based on single iron atoms dispersed on a hierarchically structured porous carbon framework. *Angew Chem Int Edit* 57:9038–9043
- Chung HT, Cullen DA, Higgins D, Sneed BT, Holby EF, More KL, Zelenay P (2017) Direct atomic-level insight into the active sites of a high-performance PGM-free ORR catalyst. *Science* 357:479–484
- Hou J, Cao C, Idrees F, Ma X (2015) Hierarchical porous nitrogen-doped carbon nanosheets derived from silk for ultrahigh-capacity battery anodes and supercapacitors. *ACS Nano* 9:2556–2564
- Zhang C, Kong R, Wang X, Xu Y, Wang F, Ren W, Wang Y, Su F, Jiang JX (2017) Porous carbons derived from hypercrosslinked porous polymers for gas adsorption and energy storage. *Carbon* 114:608–618
- Rehman S, Guo S, Hou Y (2016) Rational design of Si/SiO₂@ hierarchical porous carbon spheres as efficient polysulfide reservoirs for high-performance Li–S battery. *Adv Mater* 28:3167–3172
- Peng Y, Lu B, Chen S (2018) Carbon-supported single atom catalysts for electrochemical energy conversion and storage. *Adv Mater* 30:1801995

- [18] Jackson C, Smith GT, Inwood DW, Leach AS, Whalley PS, Callisti M, Polcar T, Russell AE, Levecque P, Kramer D (2017) Electronic metal-support interaction enhanced oxygen reduction activity and stability of boron carbide supported platinum. *Nat Commun* 8:15802
- [19] Chen HK (2001) Kinetic study on the carbothermic reduction of zinc oxide. *Scand J Metall* 30:292–296
- [20] Proietti E, Jaouen F, Lefèvre M, Larouche N, Tian J, Herranz J, Dodelet JP (2011) Iron-based cathode catalyst with enhanced power density in polymer electrolyte membrane fuel cells. *Nat Commun* 2:416
- [21] Shui J, Chen C, Grabstanowicz L, Zhao D, Liu DJ (2015) Highly efficient nonprecious metal catalyst prepared with metal–organic framework in a continuous carbon nanofibrous network. *P Natl Acad Sci* 112:10629–10634
- [22] Wang C, Chen W, Xia K, Xie N, Wang H, Zhang Y (2019) Silk-derived 2D porous carbon nanosheets with atomically-dispersed Fe–N_x–C sites for highly efficient oxygen reaction catalysts. *Small* 15:1804966
- [23] Razmjooei F, Singh KP, Bae EJ, Yu JS (2015) A new class of electroactive Fe-and P-functionalized graphene for oxygen reduction. *J Mater Chem A*. 3:11031–11039
- [24] Du C, Liu X, Ye G, Gao X, Zhuang Z, Li P, Xiang D, Li X, Clayborne AZ, Zhou X, Chen W (2019) Balancing the micro- mesoporosity for activity maximization of N-doped carbonaceous electrocatalysts for the oxygen reduction reaction. *Chemsuschem* 12:1017–1025
- [25] Zhang J, Zhao Z, Xia Z, Dai L (2015) A metal-free bifunctional electrocatalyst for oxygen reduction and oxygen evolution reactions. *Nat Nanotechnol* 10:444
- [26] Zhang R, Zhang C, Chen W (2016) FeP embedded in N, P dual-doped porous carbon nanosheets: an efficient and durable bifunctional catalyst for oxygen reduction and evolution reactions. *J Mater Chem A* 4:18723–18729
- [27] Wang YC, Lai YJ, Song L, Zhou ZY, Liu JG, Wang Q, Yang XD, Chen C, Shi W, Zheng YP, Rauf M (2015) S-doping of an Fe/N/C ORR catalyst for polymer electrolyte membrane fuel cells with high power density. *Angew Chem Int Edit* 54:9907–9910
- [28] Zhu J, Huang Y, Mei W, Zhao C, Zhang C, Zhang J, Amiin IS, Mu S (2019) Effects of intrinsic pentagon defects on electrochemical reactivity of carbon nanomaterials. *Angew Chem* 131:3899–38904
- [29] Astruc D (2017) Why is ferrocene so exceptional? *Eur J Inorg Chem* 2017(1):6–29
- [30] Gu J, Du Z, Zhang C, Yang S (2016) Pyridinic nitrogen-enriched carbon nanogears with thin teeth for superior lithium storage. *Adv Energy Mater* 6:1600917
- [31] Zhou B, Liu L, Cai P, Zeng G, Li X, Wen Z, Chen L (2017) Ferrocene-based porous organic polymer derived high-performance electrocatalysts for oxygen reduction. *J Mater Chem A* 5:22163–22169
- [32] Jin H, Zhou H, Li W, Wang Z, Yang J, Xiong Y, He D, Chen L, Mu S (2018) In situ derived Fe/N/S-codoped carbon nanotubes from ZIF-8 crystals as efficient electrocatalysts for the oxygen reduction reaction and zinc–air batteries. *J Mater Chem A*. 6:20093–20099
- [33] Liu Y, Huang B, Zhang X, Huang X, Xie Z (2019) In-situ fabrication of nitrogen-doped carbon nanosheets containing highly dispersed single iron atoms for oxygen reduction reaction. *J Power Sources* 412:125–133
- [34] Jaroniec M, Solovyov LA (2006) Improvement of the Kruk–Jaroniec–Sayari method for pore size analysis of ordered silicas with cylindrical mesopores. *Langmuir* 22:6757–6760
- [35] Guo D, Shibuya R, Akiba C, Saji S, Kondo T, Nakamura J (2016) Active sites of nitrogen-doped carbon materials for oxygen reduction reaction clarified using model catalysts. *Science* 351:361–365
- [36] Xiang D, Bo X, Gao X, Zhang C, Du C, Zheng F, Zhuang Z, Li P, Zhu L, Chen W (2019) Novel one-step synthesis of core@ shell iron–nickel alloy nanoparticles coated by carbon layers for efficient oxygen evolution reaction electrocatalysis. *J Power Sources* 438:226988
- [37] Lee CH, Lee J, Yeo S, Lee SH, Kim T, Cha HG, Eun Y, Park HJ, Kim SM, Lee KH (2017) Evolution of implanted Fe ions in SiO₂/Si wafer into uniformly sized catalyst particles for carbon nanotube forest growth. *Carbon* 123:122–128
- [38] Li W, Liang C, Qiu J, Zhou W, Han H, Wei Z, Sun G, Xin Q (2002) Carbon nanotubes as support for cathode catalyst of a direct methanol fuel cell. *Carbon* 40:787–790
- [39] Cao R, Thapa R, Kim H, Xu X, Kim MG, Li Q, Park N, Liu M, Cho J (2013) Promotion of oxygen reduction by a bio-inspired tethered iron phthalocyanine carbon nanotube-based catalyst. *Nat Commun* 4:2076
- [40] Szakacs CE, Lefèvre M, Kramm UI, Dodelet JP, Vidal F (2014) A density functional theory study of catalytic sites for oxygen reduction in Fe/N/C catalysts used in H₂/O₂ fuel cells. *Phys Chem Chem Phys* 16:13654–13661
- [41] Wang XR, Liu JY, Liu ZW, Wang WC, Luo J, Han XP, Du XW, Qiao SZ, Yang J (2018) Identifying the key role of pyridinic-N–Co bonding in synergistic electrocatalysis for reversible ORR/OER. *Adv Mater* 30:1800005

Publisher's Note Springer Nature remains neutral with regard to jurisdictional claims in published maps and institutional affiliations.